

# 1 **A new analytical method for stability analysis of rock blocks with** 2 **cavities in sub-horizontal strata by the considering eccentricity effect**

3 Xushan Shi<sup>1</sup>, Bo Chai<sup>1,3,4</sup>, Juan Du<sup>1,2,4</sup>, Wei Wang<sup>1,3,4</sup>, Bo Liu<sup>1</sup>

4 <sup>1</sup>School of Environmental Studies, China University of Geosciences, Wuhan, 430078, China

5 <sup>2</sup>Centre for severe weather and climate and hydrogeological hazards, Wuhan, 430078, China

6 <sup>3</sup>Hubei Key Laboratory of Yangtze Catchment Environmental Aquatic Science, Wuhan, 430078, China

7 <sup>4</sup>Research Center for Geohazards Monitoring and Warning in Three Gorges Reservoir, Wanzhou, 404000, China

8 *Correspondence to:* Bo Chai ([chaibo@cug.edu.cn](mailto:chaibo@cug.edu.cn)) and Juan Du ([dujuan@cug.edu.cn](mailto:dujuan@cug.edu.cn))

9 **Abstract.** The basal cavity of a rock block formed due to differential weathering is an important predisposing factor for  
10 rockfall in hard-soft interbedded rocks. Rock block falling due to the eccentricity effect with the failure modes of toppling or  
11 sliding is defined as biased rockfall in this study. Considering the non-uniform stress distribution due to the eccentricity  
12 effect, a new analytical method for three-dimensional stability analysis of biased rockfall is proposed. A set of factors of  
13 safety (*Fos*) against partial damage (compressive and tensile damage of the soft underlying layer) and overall failure  
14 (toppling and sliding of the hard rock block) are used to determine the rockfall susceptibility level. The analytical method is  
15 applied and validated with biased rockfalls on the northeast edge of the Sichuan Basin in Southwest China, where large  
16 amounts of rockfalls have developed, composed of overlying thick sandstone and underlying mudstone. The evolution  
17 process of biased rockfalls is divided into four stages, initial state, cavity formation, partial unstable and failure. The  
18 proposed method is validated by calculating *Fos* of the typical unstable rock blocks in the study area. The continuous retreat  
19 of cavity causes stress redistribution between the hard and soft rock layers. Consequently, the development of the  
20 eccentricity effect leads to damage to the underlying soft rock layer and further failure of the hard rock block. The critical  
21 cavity retreat ratio is determined to be 0.33 to classify the low and moderate rockfall susceptibility in the eastern Sichuan  
22 Basin. The proposed analytical method is effective for the early identification of biased rockfall, which is significant for  
23 rockfall prevention and risk mitigation.

## 24 **List of symbols**

25 $a$	length of the block along the $x$ direction
26 $A$	area of contact surfaces
27 $b$	width of the block along the $y$ direction
28 $c$	cohesive force of the mudstone
29 $d_i$	width of the basal cavity in a certain direction
30 $e_x$	eccentric distance along the $x$ direction
31 $e_y$	eccentric distance along the $y$ direction

32	$E_x$	horizontal seismic force along the $x$ direction
33	$Fos$	factor of safety
34	$h$	height of the block
35	$h_w$	height of the water in the fracture
36	$H_x$	water pressure along the $x$ direction
37	$I_x$	moment of inertia with respect to the $x$ -axis
38	$I_y$	moment of inertia with respect to the $y$ -axis
39	$k_e$	earthquake contribution coefficient
40	$k_1$	rainfall coefficient, taking 1 in the rainfall scenario and 0 in the non-rainfall scenario
41	$k_2$	earthquake coefficient, taking 1 in the seismic scenario and 0 in the non-seismic scenario
42	$k_3$	free surface coefficient, taking 1 for two free surfaces and 0 for three free surfaces
43	$M_{bx}$	total bending moments with respect to the $x$ -axis on the mudstone foundation
44	$M_{by}$	total bending moments with respect to the $y$ -axis on the mudstone foundation
45	$M_{bEx}$	bending moment of $E_x$ with respect to the $x$ -axis on the mudstone foundation
46	$M_{bHx}$	bending moment of $H_x$ with respect to the $x$ -axis on the mudstone foundation
47	$M_{bWx}$	bending moment of $W$ with respect to the $x$ -axis on the mudstone foundation
48	$M_{Ex}$	overturning moment provided by $E_x$ along the $x$ direction
49	$M_{Hx}$	overturning moment provided by $H_x$ along the $x$ direction
50	$M_{px}$	stabilizing moment of $p_n$ along the $x$ direction
51	$M_{W_{inx}}$	stabilizing moment provided by $W$ along the $x$ direction
52	$M_{W_{outx}}$	overturning moment provided by $W$ along the $x$ direction
53	$N_z$	total applied vertical load on the mudstone base
54	$O$	origin of the $(x, y)$ coordinates
55	$p(x, y)$	pressure magnitude at point $(x, y)$
56	$r_i$	the basal cavity retreat ratio equal to the ratio of cavity width to block width in a certain direction
57	$W$	weight of the block
58	$x$	distance to $O$ along the $x$ -axis
59	$y$	distance to $O$ along the $y$ -axis
60	$\alpha$	true dip of the contact surface
61	$\gamma_s$	unit weight of sandstone
62	$\gamma_w$	unit weight of water
63	$\theta_1$	apparent dip of $\alpha$ on plane J1
64	$\theta_2$	apparent dip of $\alpha$ on plane J2

65	$\sigma_{cmax}$	ultimate compressive strength of the mudstone
66	$\sigma_{tmax}$	ultimate tensile strength of the mudstone
67	$\tau_{max}$	ultimate shear strength of the mudstone
68	$\varphi$	friction angle of the mudstone
69	$\omega_1$	angle between the trend of the contact surface and the $x$ direction
70	$\omega_2$	angle between the trend of the contact surface and the $y$ direction

## 71 **1 Introduction**

72 Rockfall is defined as the detachment of a rock block from a steep slope along a surface, on which little or no shear  
73 displacement takes place ([Cruden and Varnes, 1996](#)). Rockfalls frequently occur in mountainous ranges, cut slopes, and  
74 coastal cliffs, and they may cause significant facility damage and casualties in residential areas and transport corridors ([Chau](#)  
75 [et al., 2003](#); [Volkwein et al., 2011](#); [Corominas et al., 2018](#)). Stability analysis of rock blocks are crucial for risk management  
76 and early warning of rockfall ([Kromer et al., 2017](#)).

77 Rockfall is widespread and poses high risk in the eastern Sichuan Basin, Southwest China ([Chen et al., 2008](#); [Chen and Tang,](#)  
78 [2010](#); [Zhang et al., 2016](#); [Zhou et al., 2017](#); [Zhou et al., 2018](#)). The rockfall in this area is attributed to the tectonic setting of  
79 Jura-type folds and the stratum sequence, which is characterized by the interbedding of hard and soft layers. An alternation  
80 of thick sandstone and thin mudstone layers is formed in the wide and gentle-angle synclines ([Zhang et al., 2015](#); [Wu et al.,](#)  
81 [2018](#)). Weathering is known to be one of the main predisposing factors for rockfall ([Jaboyedoff et al., 2021](#); [Zhan et al.,](#)  
82 [2022](#)). The cliff comprised of hard sandstone is the source of rockfall, and the underlying mudstone is more susceptible to  
83 weathering. Along with the retreat of basal cavities in the mudstone layer, the gravity centre of the overlying sandstone block  
84 moves outward relative to the mudstone. In this case, the stress distribution in the contact surface of sandstone and mudstone  
85 is non-uniform. The mudstone on the outer side bears higher compressive stress than that on the inner side. This  
86 phenomenon can be defined as an eccentricity effect, which leads to mudstone damage and failure of the overlying sandstone  
87 by toppling or sliding. This type of rockfall is defined as biased rockfall in this study (Fig. 1). Similar rockfall patterns have  
88 been widely reported in other regions, such as Joss Bay in England ([Hutchinson, 1972](#)), Okinawa Island in Japan ([Kogure et](#)  
89 [al., 2006](#)), and the Colorado Plateau of the southwestern United States ([Ward et al., 2011](#)). Retreat of the basal cavity is a  
90 main cause for the failure of the overlying block. Therefore, it is necessary to establish an analytical method, considering the  
91 development of the basal cavity, to analyse the stress distribution and stability of rock blocks, which is fundamental to the  
92 susceptibility assessment and risk control of biased rockfall.

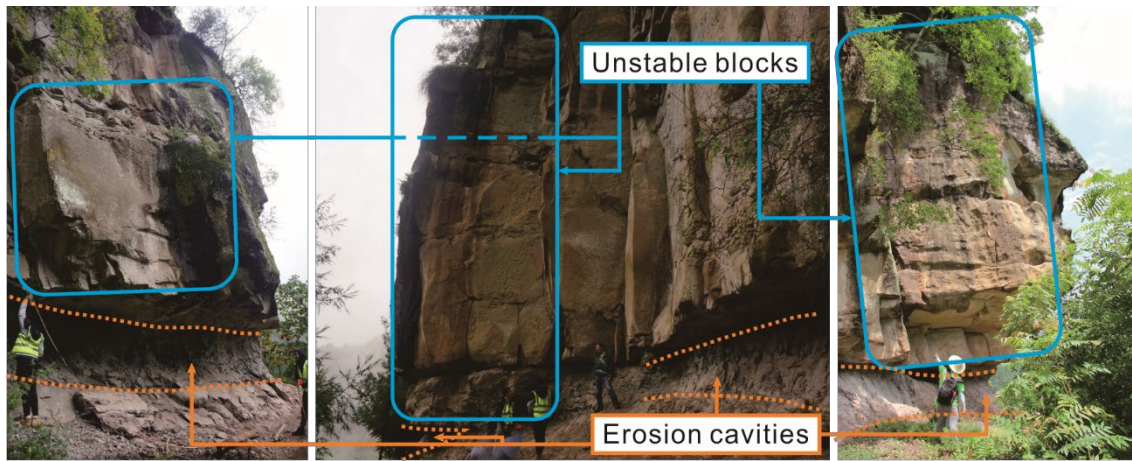
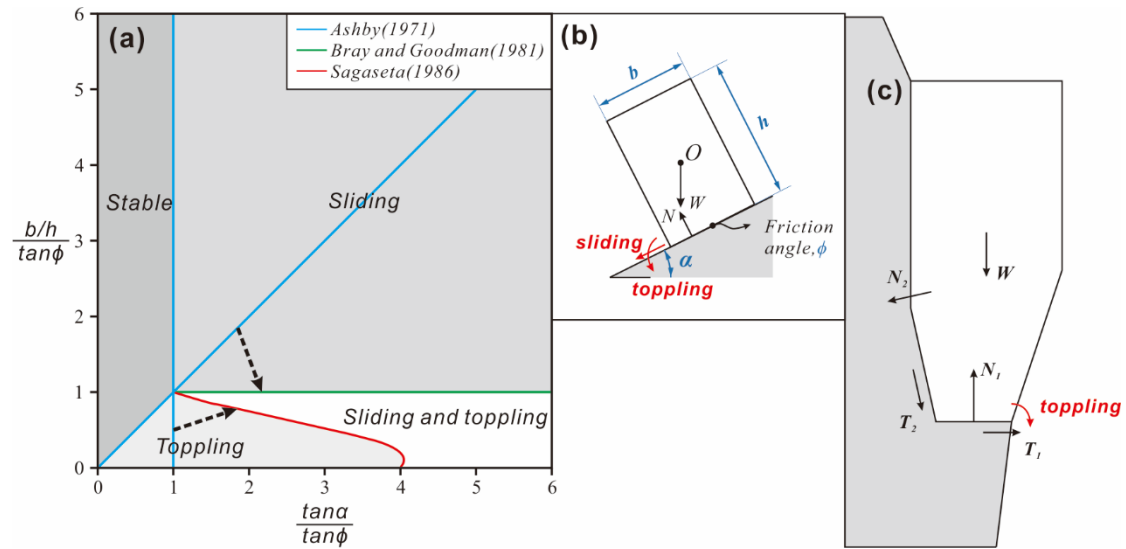


**Figure 1** Potential unstable blocks and basal cavities caused by differential weathering.

93

94

95 Rockfall stability analysis methods include statistical analysis ([Frattini et al., 2008](#); [Santi et al., 2009](#)), empirical rating  
 96 systems ([Pierson et al., 1990](#); [Ferrari et al., 2016](#)), and mechanical analysis ([Jaboyedoff et al., 2004](#); [Derron et al., 2005](#);  
 97 [Matasci et al., 2018](#)). The statistical analysis and empirical rating systems are suitable for rockfall hazard assessment at a  
 98 regional scale. The accuracy of statistical analysis depends on the completeness of rockfall inventories ([Chau et al., 2003](#);  
 99 [Guzzetti et al., 2003](#); [D'amato et al., 2016](#)). However, its application to rockfall hazards is limited due to the lack of complete  
 100 inventory data ([Budetta and Nappi, 2013](#); [Malamud et al., 2004](#)). Empirical and semi-empirical rating systems are used  
 101 where site-specific rockfall inventories are either unavailable or unreliable. Therefore, rockfall susceptibility can be assessed  
 102 by heuristic ranking of selected predisposing factors ([Frattini et al., 2008](#); [Budetta, 2004](#)). Mechanical analysis based on  
 103 static equilibrium theory is the main method to analyse the stability of site-specific rockfall using the factor of safety ( $Fos$ ).  
 104 [Ashby \(1971\)](#) conducted stability analysis with a parallelepiped block resting on an inclined plane (Fig. 2a), and the solution  
 105 was subsequently modified by [Bray and Goodman \(1981\)](#) and [Sagaseta \(1986\)](#). [Kogure et al. \(2006\)](#) utilized a cantilever  
 106 beam model to determine the critical state of limestone cliffs. [Frayssines and Hantz \(2009\)](#) proposed the limit equilibrium  
 107 method (LEM) to predict block stability against sliding and toppling in steep limestone cliffs (Fig. 2c). [Chen and Tang \(2010\)](#)  
 108 established a stability analysis method of three types of unstable rocks in the Three Gorges Reservoir area with the LEM.  
 109 [Alejano et al. \(2015\)](#) studied the influence of rounding of block corners on the block stability. [Zhang et al. \(2016\)](#) defined  
 110  $Fos$  based on fracture mechanics and studied the progressive failure process by analysing crack propagation. [Alejano et al.](#)  
 111 [\(2010\)](#) and [Pérez-Rey et al. \(2021\)](#) deduced a formula for  $Fos$  of blocks with more complex geometry.



112

113 **Figure 2** Traditional force analysis diagrams of the rock block. (a) and (b) are stability analysis diagrams of rock blocks under dynamic  
 114 conditions, resting on an inclined plane with a dip angle of  $\alpha$ . The rock block is generalized as a cuboid with dimensions  $b \times h$  and weight  
 115  $W$  (as modified from [Ashby \(1971\)](#), [Bray and Goodman \(1981\)](#) and [Sagaseta \(1986\)](#)). (c) Force description of the toppling model proposed  
 116 by [Frayssines and Hantz \(2009\)](#). In the above assumptions,  $N$ ,  $T$ , and  $W$  are regarded as forces applied at a point.

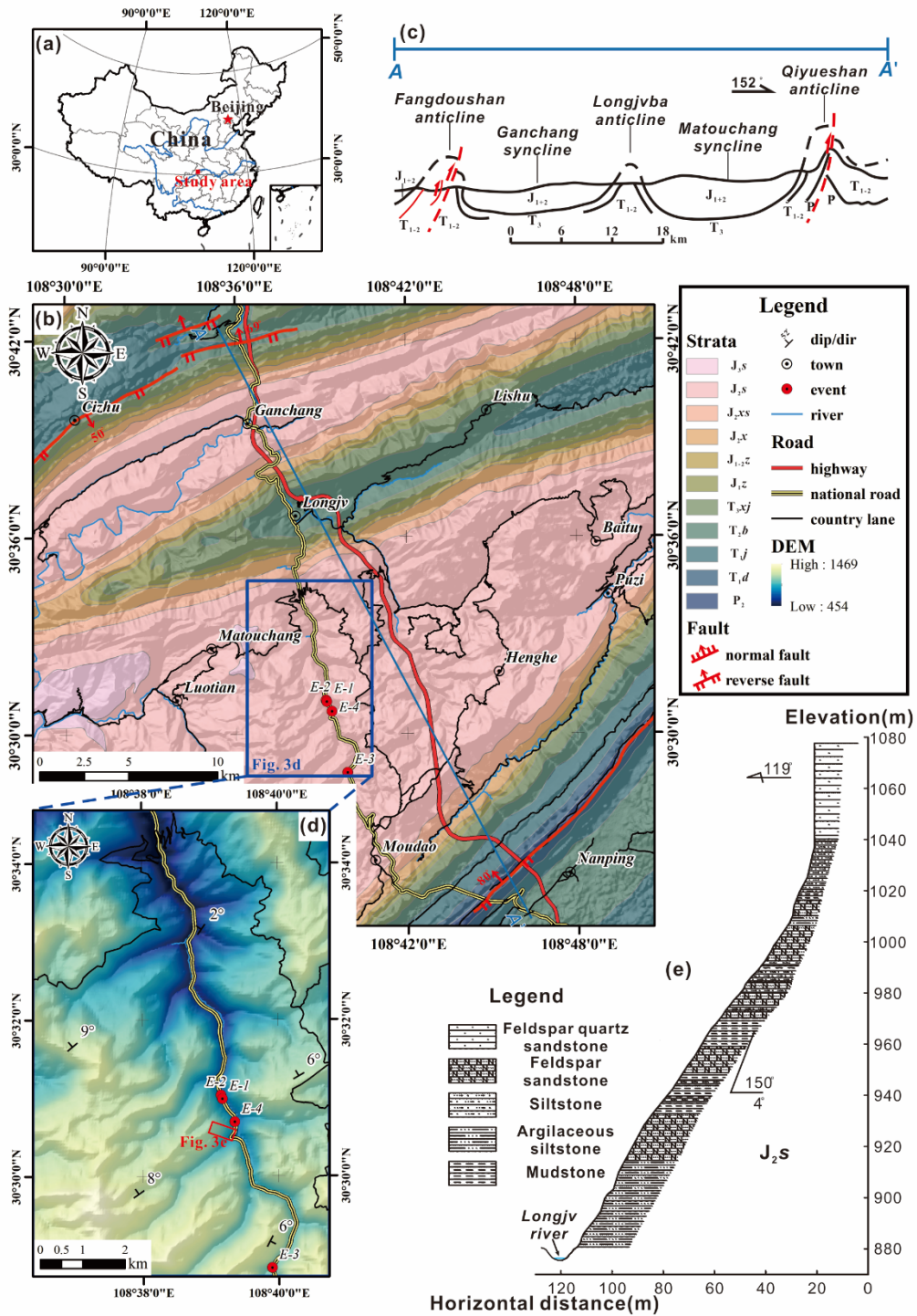
117 The supporting force on the contact surface is assumed to be applied at a point in the current LEM methods (i.e.,  $N$  in Fig. 2  
 118 b and c). However, the supporting force is actually a distributed force. The cavity generates an eccentricity effect on the  
 119 overlying rock block and results in a non-uniform distribution of the supporting force on the contact surface, which is not  
 120 considered in the traditional LEM. Furthermore, most studies simplified the three-dimensional geometry of the rock block by  
 121 one cross-section, which is used to represent the critical features of the slope structure. Nevertheless, for natural blocks with  
 122 basal cavities, the cavities usually present different depths along different directions ([Pérez-Rey et al., 2021](#)). Therefore, a  
 123 three-dimensional model is necessary to calculate the accurate stability. In addition, when a block has multiple free faces and  
 124 a complex structure, its potential failure is dominated by different modes, including rock mass damage and overall block  
 125 failure. Therefore, the probable failure modes should be determined prior to the calculation of  $FOS$ .

126 Based on rockfall investigation in the Eastern Sichuan Basin, China, the main objective of this study was to propose a new  
 127 three-dimensional method for the determination of failure modes and  $FOS$  of biased rockfall, considering the non-uniform  
 128 force distribution on the contact surfaces. Compared with the traditional LEM method, this study takes into account the  
 129 partial damage of the underlying soft rock and the overall instability of the overlying hard rock blocks, and can evaluate the  
 130 stability of biased rockfall more comprehensively.  $FOS$  of the typical unstable rock blocks in the study area are calculated to  
 131 validate the proposed method. In addition, the critical cavity retreat ratio in this area is analysed. This study is an extension  
 132 of the basic LEM for rockfall, which can promote the accuracy of rockfall stability analysis and facilitate rockfall prevention  
 133 and risk mitigation.

## 134 **2 Study area**

### 135 **2.1 Geological setting**

136 The study area is located on the northeastern edge of the Sichuan Basin, China (Fig. 3a). Continuous erosion processes  
137 generate moderate-low mountain and valley landforms ([Yu et al., 2021](#)). The tectonic structure of this area is characterized  
138 by a series of ENE anticlines and synclines (Fig. 3b, c). In the anticline area, the rock layers dip relatively steeply, where  
139 translational rockslides are the main mode of slope failure. The syncline area is dominated by gently dipping strata and is  
140 prone to rockfall ([Zhou et al., 2018](#)). The study area is located in the core of the Matouchang syncline, where the rock layers  
141 are sub-horizontal (Fig. 3d, e). In this valley, due to the longstanding fluvial incision, the relative relief is approximately 500  
142 m and the valley flanks are extremely steep (Fig. 3e). In addition, the toes of the hill slopes are reshaped because of the  
143 construction of the G318 national road, which is the main traffic line and is always threatened by rockfalls dropping from  
144 steep rock slopes (shown in Fig. 3d and Table 1).



145

146 **Figure 3** (a) Location of the study area in China; (b) geological map of the study area; (c) tectonic sketch profile of A-A', whose location

147 is showed in Fig. 3b; (d) rockfall-prone segment and key investigation areas. The red dots are the positions of historical rockfall events,

148 corresponding to the numbers in Table 1; (e) Geological cross-section of the hillslope in the Jitougou section of G318 national road, which  
 149 is marked by a red rectangle in Fig. 3d.

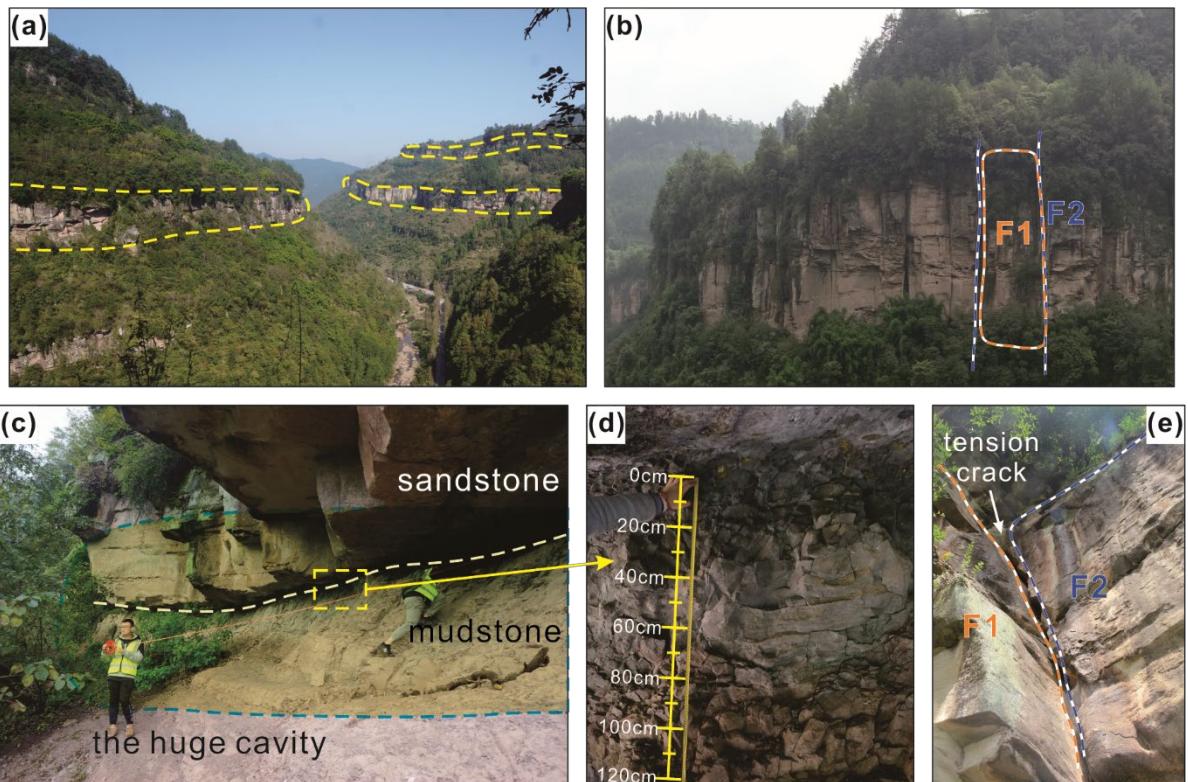
150 **Table 1** Historical rockfall events along G318 national road in the study area

No	Location	Time of occurrence (GMT+8)	Volume [m <sup>3</sup> ]	Consequence
E-1	K1698+900	2014-05 to 06*	Unknown	The power transmission facilities outside the road were smashed.
E-2	K1699+000	2015-02-14 23:00	About 240	A passing truck was stuck and two people dead.
E-3	K1690+700	2015-06-16	Unknown	The road was interrupted for a day.
E-4	K1698+400	2015-06-18 09:00	About 200	A vehicle was crashed into a gully and four people dead.

151 \*Note: The exact time is unknown.

## 152 2.2 Rockfall characteristics

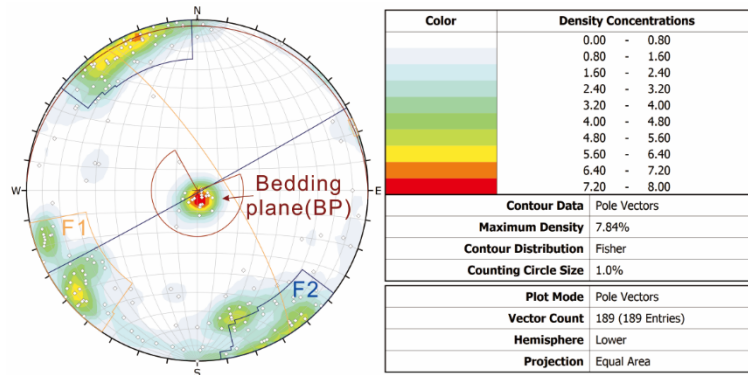
153 The slopes in the study area consist of a sub-horizontally interbedded sandstone and mudstone layer. Therefore, there are  
 154 multiple layers of potentially unstable rock blocks in the hill slopes (Fig 4a). The thick sandstone has two sets of sub-vertical  
 155 joints (Fig. 5), which cut the rock mass into blocks as the potential rockfall source (Fig. 4b). Cavities have formed in the  
 156 underlying mudstone layer (Fig. 4c, d). Joints and bedding planes (BP) constitute the detachment surfaces between the  
 157 blocks and steep slope (Fig. 4e). The eccentricity effect produced by the mudstone cavity plays an important role in the  
 158 evolution process of rockfall. When the basal mudstone cannot provide adequate supporting force, the blocks detach from  
 159 the steep slope, and biased rockfall occurs. Sliding and toppling are two possible failure modes of biased rockfall.



160



161 **Figure 4** Characteristics of biased rockfalls in the study area. (a) Multiple-layers of rockfall sources, which is consist of thick sandstone. (b)  
 162 Two sets of sub-vertical joints (F1 and F2) recognized by the UAV photos. (c) Large basal cavity developed in the underlying mudstone.  
 163 (d) Dense fractures on the mudstone surface generated by weathering and compression. (e) Vertical tension crack in the rear of the block,  
 164 through which precipitation can infiltrate.  
 165 According to the historical rockfall events in this area, precipitation is considered a triggering effect of rock instability. The  
 166 precipitation mainly infiltrates along the sub-vertical joints or cracks of the sandstone (Fig. 4e). However, the drainage of  
 167 fissure water is hysteretic due to the obstruction of basal mudstone. Therefore, transient steady flow exists in vertical cracks  
 168 during heavy rainfall, and the hydrostatic pressure triggers the detachment of rock blocks. Thus, typical scenarios (such as  
 169 rainfall intensity and earthquake) need to be considered in the stability analysis model.



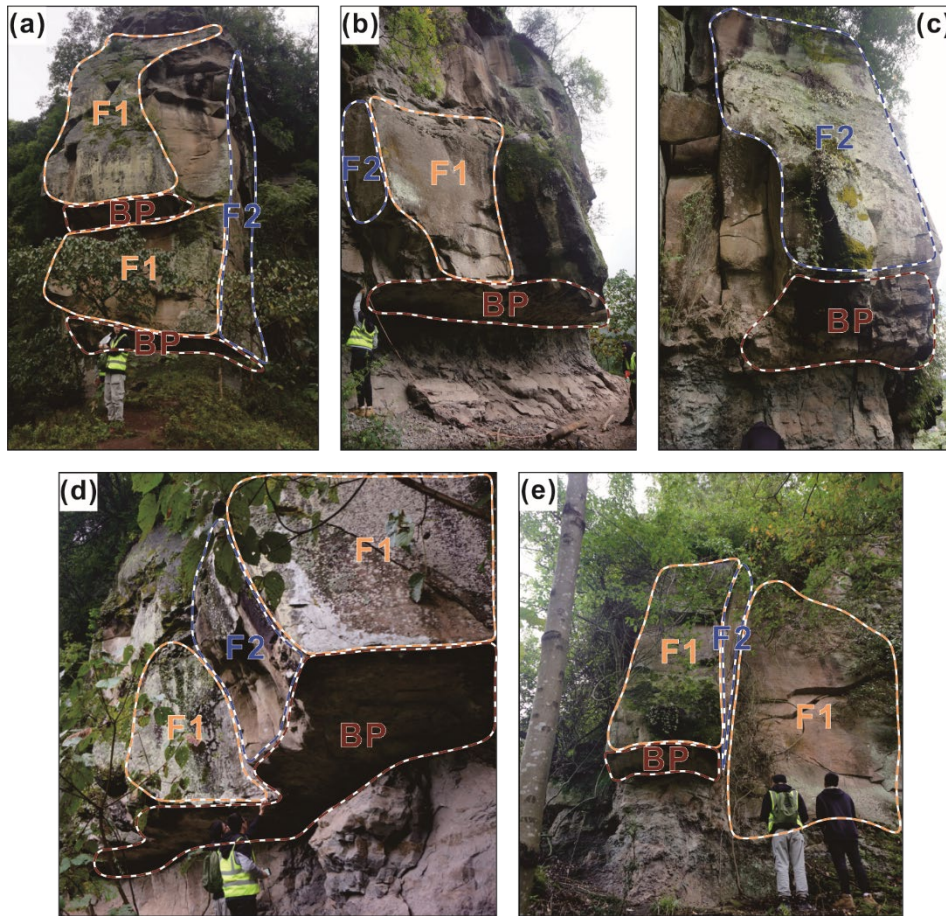
170  
 171 **Figure 5** Stereo net produced using compass-clinometer survey data, which shows the densities and orientations of five clusters. The data  
 172 were collected in the rockfall-prone area shown in Fig. 3d.

### 173 3 Calculation method

#### 174 3.1 Geological models and assumptions

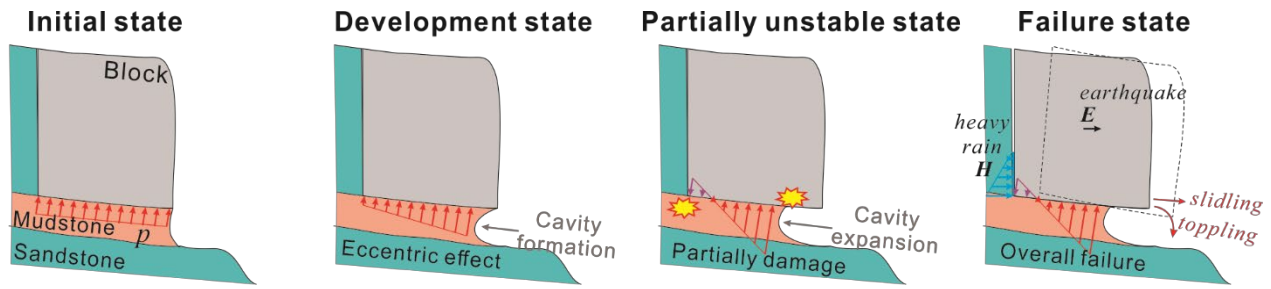
175 A detailed geological investigation of unstable rock blocks was carried out in the study area (Fig. 6). The geological model  
 176 of the rock block is mainly composed of the overlying sandstone and the underlying mudstone. The sandstone block is  
 177 assumed to be a rigid body, which is divided by two sets of orthogonal vertical smooth joints without friction resistance.  
 178 According to the relatively persistent sub-vertical fractures observed in the field, the vertical joints are assumed to be fully  
 179 persistent in the geological model. The sandstone block is assumed to be a complete body without persistent discontinuity,  
 180 and it will not disintegrate before it falls. Due to the cavity in mudstone, the contact surface between sandstone and  
 181 mudstone exhibits an eccentricity effect where non-uniform stresses are distributed at different positions. Mudstone is  
 182 mainly loaded by compressive stress and tensile stress. When the compressive stress of mudstone exceeds its strength on the  
 183 outer side, some initial damage appears. The effective contact surface between mudstone and sandstone is reduced, which  
 184 aggravates the non-uniform distribution of stress. In this way, the ability of mudstone to resist the sliding and toppling of  
 185 overlying sandstone is reduced. In the field, compression deformation of mudstone can be observed, which usually manifests

186 as micro-fractures and cleavages (Fig. 4d). The deformation is very slight and slow in the short term. In addition, the LEM is  
187 essentially a force/stress approach that does not take into account the deformation. Therefore, in this study, it is assumed that  
188 the mudstone is not subjected to deformation. The rock block remains in the state of static equilibrium prior to the final  
189 overall failure. Fig. 7 displays the four evolution stages of biased rockfall. In the initial stage, the base cavity has not yet  
190 formed, and the normal force acting on the contact surface is uniform in different positions. The eccentricity effect leads to a  
191 non-uniform supporting force as the cavity grows, and partial damage gradually develops when the non-uniform stress  
192 exceeds the compressive or tensile strength of the mudstone. Under the triggering effects of rainfall or earthquakes, the rock  
193 blocks are separated by sliding or toppling.



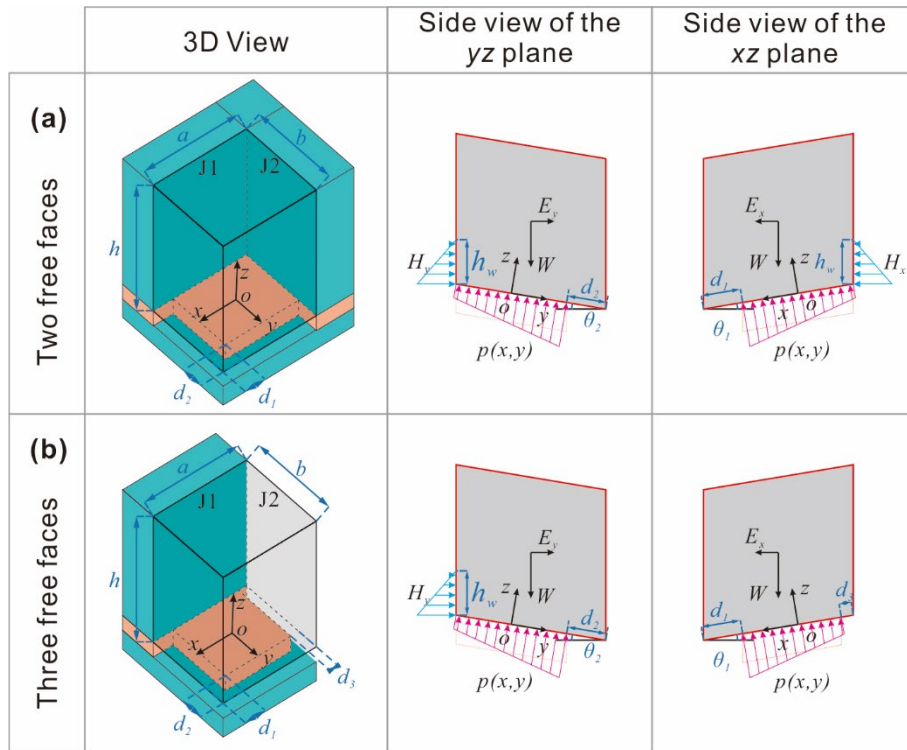
194

195 **Figure 6** The unstable blocks were labelled W02, W08, W18, W04, and W21, which are detached by the dominating discontinuities in Fig.  
196 5. Basal cavities can be identified under the bedding planes of sandstone.



197  
198 **Figure 7** The evolution process of rock blocks from stable state to failure.

199 Fig. 8 represents the mechanical model of the force equilibrium analysis of a rock block with two or three free faces. The  
200 rock block (the overlying sandstone) is generalized as a parallelepiped block. The underlying mudstone is impermeable, so  
201 rainfall can fill the joints and transmit horizontal hydrostatic pressure. The shear strength of the underlying mudstone is  
202 assumed to obey the Mohr–Coulomb criterion. Rainfall and earthquakes decrease *Fos* by generating hydrostatic pressure *H*  
203 in the vertical crack and horizontal seismic force *E* on the block.  
204 A Cartesian coordinate system is established in three-dimensional space for the force analysis. The origin *O* is located at the  
205 centre of the contact surface between sandstone and mudstone. For the case with two free surfaces, the orientation of the free  
206 surfaces is set to be the positive direction of the *x*-axis and *y*-axis. For the case with three free surfaces, the negative  
207 direction of the *x*-axis is also a free surface. Joint J2 is perpendicular to the *x*-axis, and joint J1 is perpendicular to the *y*-axis.



208

209 **Figure 8** Diagram of the force equilibrium analysis of the rock block model. (a) and (b) represent the case of unstable rock blocks with  
 210 two or three free vertical surfaces, respectively.

## 211 3.2 Calculation processes

### 212 3.2.1 Stress distribution at the block base

213 The following formulas are used to calculate the apparent dip of  $\alpha$  ( $\theta_1$  and  $\theta_2$ ):

$$214 \theta_1 = \arctan(\tan \alpha \cdot \cos \omega_1) \quad (1)$$

$$215 \theta_2 = \arctan(\tan \alpha \cdot \cos \omega_2) \quad (2)$$

216 where  $\omega_1$  and  $\omega_2$  are the angles between the trend of the contact surface and the  $x$  direction or  $y$  direction, respectively.

217 As shown in Fig. 8b, with respect to the  $x$ -axis, gravity, seismic forces, and hydrostatic pressure create a non-symmetrical  
 218 stress distribution on the foundation. The bending moment of gravity with respect to the  $x$ -axis ( $M_{bWx}$ ) is

$$219 M_{bWx} = W \cdot \frac{d_1 - d_3}{2} \cos \theta_1 \quad (3)$$

220 Assuming that the height of the water in the fracture is  $h_w$ , the hydrostatic pressure along the  $x$  direction ( $H_x$ ) and its  
 221 bending moment ( $M_{bHx}$ ) are respectively expressed as

$$222 H_x = \frac{\gamma_w h_w^2}{2} (b - d_2) \quad (4)$$

$$223 M_{bHx} = \int_{\frac{b-d_2}{2}}^{\frac{b-d_2}{2}} \int_0^{h_w \cos \theta_1} \gamma_w \left( h_w - \frac{z}{\cos \theta_1} \right) \left( \frac{z}{\cos \theta_1} + \frac{a - d_1 - d_3}{2} \cdot \sin \theta_1 \right) dz dy \quad (5)$$

224 The horizontal seismic force along  $x$  direction ( $E_x$ ) and its bending moment ( $M_{bEx}$ ) are respectively expressed as

$$225 E_x = k_e W \quad (6)$$

$$226 M_{bEx} = E_x \left( \frac{h}{2} - \frac{d_1 - d_3}{2} \sin \theta_1 \right) \quad (7)$$

227 The total applied vertical load ( $N_z$ ) and the total bending moments along the  $x$  direction ( $M_{bx}$ ) can be derived as

$$228 N_z = W \cos \alpha - (H_x \cdot k_1 \cdot k_3 + E_x \cdot k_2) \sin \theta_1 - (H_y \cdot k_1 + E_y \cdot k_2) \sin \theta_1 \quad (8)$$

$$229 M_{bx} = M_{bWx} + M_{bHx} \cdot k_1 \cdot k_3 + M_{bEx} \cdot k_2 \quad (9)$$

230 where  $k_1$ ,  $k_2$  and  $k_3$  are the coefficients set to make Eq. (8) and Eq. (9) compatible with different calculation scenarios.

231 Therefore, Eqs. (8) and (9) and the following formulas can be expressed in a unified form. In the natural scenario,  $k_1$  and  $k_2$

232 are both equal to 0. In the rainfall scenario,  $k_1 = 1$ . In the earthquake scenario,  $k_2 = 1$ . For the case of two free faces,  $k_3 =$

233 1. For the case of three free surfaces,  $k_3 = 0$ .

234 Based on bending theory ([Adrian, 2010](#)), the eccentricity distance along the  $x$  direction ( $e_x$ ) can be expressed as

$$235 e_x = \frac{M_{bx}}{N_z} = \frac{M_{bWx} + M_{bHx} \cdot k_1 \cdot k_3 + M_{bEx} \cdot k_2}{W \cos \alpha - (H_x \cdot k_1 \cdot k_3 + E_x \cdot k_2) \sin \theta_1 - (H_y \cdot k_1 + E_y \cdot k_2) \sin \theta_1} \quad (10)$$

236 The same method can be used to obtain  $e_y$ :

$$237 \quad e_y = \frac{M_{by}}{N_z} = \frac{M_{bWy} + M_{bHy} \cdot k_1 + M_{bEy} \cdot k_2}{W \cos \alpha - (H_x \cdot k_1 \cdot k_3 + E_x \cdot k_2) \sin \theta_1 - (H_y \cdot k_1 + E_y \cdot k_2) \sin \theta_1} \quad (11)$$

238 According to the stress distribution of a rectangular shaped foundation ([Adrian, 2010](#)), the stress in the  $(x, y)$  coordinates,  
239  $p(x, y)$ , is

$$240 \quad p(x, y) = \frac{N}{A} + \frac{Ne_x}{I_y} x + \frac{Ne_y}{I_x} y \quad (12)$$

241 with the formulas

$$242 \quad I_x = \frac{(a - d_1)(b - d_2)^3}{12} \quad (13)$$

$$243 \quad I_y = \frac{(b - d_2)(a - d_1)^3}{12} \quad (14)$$

$$244 \quad A = (a - d_1 - d_3)(b - d_2) \quad (15)$$

245 By substituting Eq. (13-15) into Eq. (12),  $p(x, y)$  can be derived as

$$246 \quad p(x, y) = \frac{N}{A} \left[ 1 + \frac{12e_x}{(a - d_1 - d_3)^2} x + \frac{12e_y}{(b - d_2)^2} y \right] \quad x \in \left[ -\frac{a - d_1 - d_3}{2}, \frac{a - d_1 - d_3}{2} \right], y \in \left[ -\frac{b - d_2}{2}, \frac{b - d_2}{2} \right] \quad (16)$$

247  $p_{max}$  and  $p_{min}$  can be derived from Eq. (16) as

$$248 \quad p_{max} = p \left( \frac{a - d_1 - d_3}{2}, \frac{b - d_2}{2} \right) \quad (17)$$

$$249 \quad p_{min} = p \left( -\frac{a - d_1 - d_3}{2}, -\frac{b - d_2}{2} \right) \quad (18)$$

250 The mudstone foundation has both compressive strength and tensile strength, so the value of  $p(x, y)$  is modified to obtain  
251 the two piecewise functions

$$252 \quad p_p(x, y) = \begin{cases} \sigma_{cmax}, & p(x, y) \geq \sigma_{cmax} \\ p(x, y), & 0 < p(x, y) \leq \sigma_{cmax} \\ 0, & p(x, y) < 0 \end{cases} \quad (19)$$

$$253 \quad p_n(x, y) = \begin{cases} 0, & p(x, y) < -\sigma_{tmax} \\ p(x, y), & -\sigma_{tmax} \leq p(x, y) < 0 \\ 0, & p(x, y) \geq 0 \end{cases} \quad (20)$$

254 Here,  $p_p(x, y)$  provides support normal force for the overlying sandstone, and  $p_n(x, y)$  provides tension force.

### 255 3.2.2 Calculation of factors of safety

256 According to the principle of friction, the ultimate shear strength  $\tau_{max}$  is

$$257 \quad \tau_{max} = \int_{-\frac{a-d_1-d_3}{2}}^{\frac{a-d_1-d_3}{2}} \int_{-\frac{b-d_2}{2}}^{\frac{b-d_2}{2}} [p_p(x, y) \tan \varphi + c] dy dx \quad (21)$$

258 Therefore,  $Fos$  against sliding,  $Fos_{sl}$ , can be defined as

$$259 \quad FOS_{sl} = \frac{S_{stabilizing}}{S_{sliding}} = \frac{\tau_{max}}{W|\sin \alpha_s| + H_x \cdot \cos \omega_s \cdot \cos \alpha_s \cdot k_1 \cdot k_3 + H_y \cdot |\sin \omega_s| \cdot \cos \alpha_s \cdot k_1 + E \cdot \cos \alpha_s \cdot k_2} \quad (22)$$

260 When the block can slide freely,  $\alpha_s = \alpha$ ,  $\omega_s = 0$ ; when the block is constrained to slide along a joint plane (e.g., J1),  $\alpha_s =$   
 261  $\theta_1$  or  $\theta_2$ ,  $\omega_s = \omega_1$  or  $\omega_2$ . For the case of an anaclinal slope, the sliding direction is opposite to the free surface. Therefore,  
 262 the rock block does not slide, and  $FOS_{sl}$  is not considered in the model.

263 With regard to stability against toppling, along the  $x$  direction, the part of the block above the mudstone base provides the  
 264 stabilizing moment  $M_{W_{inx}}$ , and the part of the block above the cavity provides the overturning moment  $M_{W_{outx}}$ . When  
 265 tension exists, there is an additional stabilizing moment.  $M_{px}$ ,  $M_{W_{inx}}$ ,  $M_{W_{outx}}$  and  $M_{px}$  can be derived as

$$266 \quad M_{W_{inx}} = W \frac{a - d_1}{a} \cos \theta_1 \cdot \left( \frac{a - d_1}{2} \right) \quad (23)$$

$$267 \quad M_{W_{outx}} = W \frac{d_1}{a} \cos \theta_1 \cdot \frac{d_1}{2} \quad (24)$$

$$268 \quad M_{px} = - \int_{-\frac{b-d_2}{2}}^{\frac{b-d_2}{2}} \int_{\frac{a-d_1-d_3}{2}}^{\frac{a-d_1-d_3}{2}} p_n(x, y) \cdot \left( \frac{a}{2} - d_1 - x \right) dx dy \quad (25)$$

269 and  $M_{Hx}$  and  $M_{Ex}$  can be derived as

$$270 \quad M_{Hx} = \int_{-\frac{b-d_2}{2}}^{\frac{b-d_2}{2}} \int_0^{h_w \cos \theta_1} \gamma_w \left( h_w - \frac{z}{\cos \theta_1} \right) \left( \frac{z}{\cos \theta_1} + (a - d_1) \sin \theta_1 \right) dz dy \quad (26)$$

$$271 \quad M_{Ex} = E_x \left( \frac{h}{2} + \left( \frac{a}{2} - d_1 \right) \sin \theta_1 \right) \quad (27)$$

272 Therefore, the  $Fos$  against toppling along the  $x$  direction,  $FOS_{tox}$ , results in

$$273 \quad FOS_{tox} = \frac{M_{stabilizing}}{M_{overturning}} = \frac{M_{W_{inx}} + M_{px}}{M_{W_{outx}} + M_{Hx} \cdot k_1 \cdot k_3 + M_{Ex} \cdot k_2} \quad (28)$$

274 Similarly,  $FOS_{toy}$  can be obtained as

$$275 \quad FOS_{toy} = \frac{M_{stabilizing}}{M_{overturning}} = \frac{M_{W_{iny}} + M_{py}}{M_{W_{outy}} + M_{Hy} \cdot k_1 + M_{Ey} \cdot k_2} \quad (29)$$

276 The smaller value is selected as the  $Fos$  of the toppling failure mode  $FOS_{to}$ :

$$277 \quad FOS_{to} = \min(FOS_{tox}, FOS_{toy}) \quad (30)$$

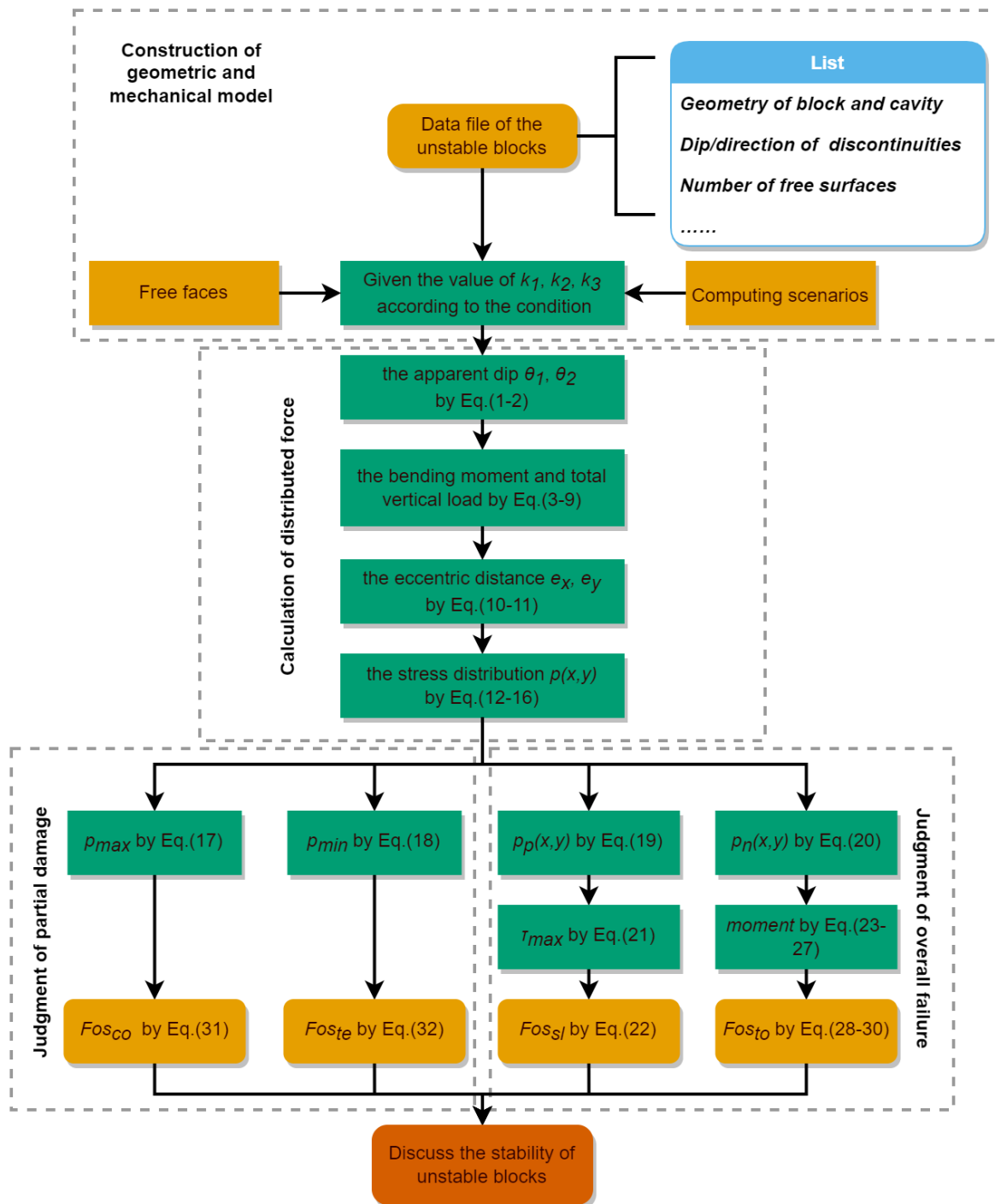
278 When the stress on mudstone exceeds its strength, it causes partial damage and decreases the stability of the rock block.

279 Therefore,  $Fos$  with the consideration of compressive strength ( $FOS_{co}$ ) and tensional strength ( $FOS_{te}$ ) can be derived as

$$280 \quad FOS_{co} = \frac{\sigma_{cmax}}{p_{max}} \quad (31)$$

$$281 \quad FOS_{te} = \frac{\sigma_{tmax}}{-p_{min}} \quad (32)$$

282  $FOS_{co}$  and  $FOS_{te}$  represent the current damage degree of mudstone due to compressive stress and tensile stress, respectively.  
283 When the stress exceeds the ultimate strength, the strength of the mudstone is reduced to the residual value, and the initial  
284 deformation appears. The ability of mudstone to provide resistance to the sliding and toppling of sandstone blocks is thus  
285 reduced, and  $FOS_{sl}$  and  $FOS_{to}$  subsequently decline. The smaller the value of  $FOS_{co}$  and  $FOS_{te}$ , the greater the damage to the  
286 underlying mudstone. The effective contact area between sandstone and mudstone becomes smaller as the development of  
287 compressive and tension damage, which significantly affects the stability of the overlying sandstone block.  
288 Finally, four  $FOS$  of unstable rock block are obtained.  $FOS_{sl}$  and  $FOS_{to}$  are routine indicators directly representing the  
289 stability of sandstone blocks.  $FOS_{co}$  and  $FOS_{te}$  are two indicators proposed in this study for the stability analysis of biased  
290 rockfall, which describe the damage state of the underlying mudstone base. It is necessary to simultaneously consider four  
291  $FOS$  to evaluate the stability of unstable biased rockfall. The entire calculation process is shown in Fig. 9.



292  
293

Figure 9 Calculation process of  $Fos$  of the unstable rock blocks.



#### 294 4 Parameters and results

295 A detailed field investigation was carried out in the source area of rockfall (Fig. 3d). The size of the blocks was determined  
296 by on-site measurement with tape and a laser rangefinder. The basal cavities in mudstone were measured with a steel ruler,  
297 and the morphological characteristics of mudstone foundation were mainly described with the average erosion depth of the  
298 cavity. The attitude of discontinuities was measured by compass. The mechanical parameters for the  $Fos$  calculation of rock  
299 blocks were determined by referring to published literature and investigation reports in this area. The unit weight of the  
300 sandstone block ( $\gamma_s$ ) is 25 kN/m<sup>3</sup> (Tang et al., 2010), the friction angle of the contact surface ( $\varphi$ ) is set to 25° and the  
301 cohesion ( $c$ ) is set to 70 kPa (Zhang et al., 2016). Because of the strength degradation of mudstone foundations due to  
302 intense weathering, the maximum compressive stress of mudstone ( $\sigma_{cmax}$ ) is replaced by the bearing capacity of mudstone  
303 foundations (2300 kPa), which is obtained through plate load tests in adjacent areas (Zheng et al., 2021). In addition, the  
304 maximum tensile stress of mudstone ( $\sigma_{tmax}$ ) is value as one-ninth of  $\sigma_{cmax}$ . The height of the water level ( $h_w$ ) is set to be  
305 one-third of  $h$ , and an earthquake contribution coefficient  $k_e$  of 0.05 is considered in stability calculations. The data obtained  
306 from the field survey were organized according to the coordinate system of the geological model in Section 3.1, and  $Fos$  was  
307 calculated according to the calculation steps in Section 3.2. The calculated geometric parameters and  $Fos$  results are shown  
308 in Table 2.

Table 2 Geometric parameters of rock blocks in the study area and  $Fos$  results.

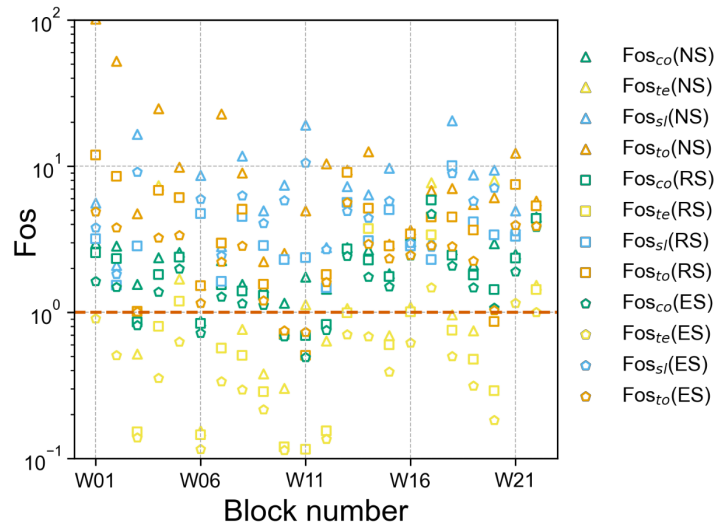
Block number	Free faces	$h$ [m]	$a$ [m]	$b$ [m]	$d_1$ [m]	$d_2$ [m]	$d_3$ [m]	$\alpha$ [°]	Dip direction [°]		NS (Natural scenario)			RS (Rainfall scenario)			ES (Earthquake scenario)							
									BD	J1	J2	$Fos_{te}$	$Fos_{co}$	$Fos_{st}$	$Fos_{to}$	$Fos_{min}$	$Fos_{te}$	$Fos_{co}$	$Fos_{st}$	$Fos_{to}$	$Fos_{te}$	$Fos_{co}$	$Fos_{st}$	$Fos_{to}$
W01	3	23	7.2	6.1	0.65	0.25	0.17	6	78	7	97	-	2.99	5.61	101.54	2.99	-	2.56	3.18	11.91	0.90	1.63	3.81	4.88
W02	3	23	6.42	5.25	0.78	0.4	0.31	16	148	51	141	-	2.84	2.10	52.28	2.10	-	2.33	1.54	8.49	0.51	1.48	1.82	3.79
W03	2	20	3.5	2.6	0.84	0.55	-	7	341	53	143	0.52	1.56	16.53	4.72	0.52	0.15	0.86	2.83	1.02	0.14	0.81	9.12	1.01
W04	2	19	4.6	4.6	0.62	0.77	-	7	273	65	155	7.35	2.37	-	24.74	2.37	0.80	1.81	-	6.83	0.35	1.38	-	3.23
W05	2	15	16.7	5.6	2.13	1.36	-	5	283	50	140	1.70	2.57	-	9.86	1.70	1.19	2.39	-	6.10	0.63	1.99	-	3.36
W06	3	20	16.7	9.7	7.5	4.2	3.9	5	302	226	316	0.15	0.87	8.67	1.53	0.15	0.15	0.84	4.73	1.52	0.12	0.72	5.96	1.16
W07	2	22	9.2	3.7	0.64	0.8	-	12	324	315	405	-	2.27	2.82	22.86	2.27	0.57	1.55	1.62	2.97	0.34	1.28	2.44	2.21
W08	2	23	12	7.9	2	1.9	-	3	317	332	422	0.76	1.55	11.75	8.99	0.76	0.51	1.40	4.51	5.09	0.29	1.14	6.29	2.84
W09	2	18	8.4	6	0.9	2.5	-	8	60	335	425	0.38	1.48	4.98	2.23	0.38	0.29	1.30	2.87	1.56	0.22	1.12	4.08	1.20
W10	2	23	5.7	3.3	1.3	0.85	-	5	329	313	403	0.30	1.16	7.41	2.53	0.30	0.12	0.71	2.30	0.71	0.11	0.68	5.84	0.75
W11	3	22	1.1	2	0.1	0.64	0.1	4	327	120	210	1.13	1.74	19.08	4.97	1.13	0.12	0.69	2.37	0.51	0.07	0.49	10.57	0.73
W12	2	25	3.9	4	0.74	0.96	-	12	355	297	387	0.64	1.44	2.78	10.36	0.64	0.15	0.82	1.48	1.81	0.14	0.75	2.70	1.61
W13	2	12	11.9	10.9	3	2.28	-	7	36	73	163	1.06	2.77	7.28	9.39	1.06	0.99	2.71	5.63	9.02	0.70	2.41	4.93	5.65
W14	3	19	13	5	0	1.1	0	8	296	73	163	-	2.67	6.40	12.57	2.67	3.75	2.28	3.09	5.15	0.68	1.75	4.41	2.94
W15	2	18	22	6	8.3	0	-	8	351	200	290	0.70	1.84	9.74	2.93	0.70	0.60	1.75	5.03	2.83	0.39	1.50	5.79	2.34
W16	3	11	5.2	7.6	0	2.9	0	13	42	144	234	1.09	3.04	3.46	3.65	1.09	1.01	2.96	2.84	3.45	0.62	2.45	2.98	2.45
W17	3	7	8	2	0	0.56	0	20	30	156	246	7.71	6.72	3.07	6.83	3.07	3.40	5.87	2.29	4.49	1.48	4.70	2.81	2.86
W18	2	12	8.5	4.5	1.61	1.27	-	2	252	253	343	0.97	2.66	20.49	7.05	0.97	0.75	2.46	10.06	4.50	0.50	2.08	8.90	2.82
W19	2	15	4.2	5.2	1.6	0.68	-	5	28	56	146	0.75	2.12	8.71	5.49	0.75	0.48	1.80	4.17	3.66	0.31	1.48	5.79	2.24
W20	3	15	1.8	1.7	0.23	0.5	0.3	4	20	63	153	7.96	2.95	9.44	6.08	2.95	0.29	1.43	3.39	0.87	0.18	1.07	7.12	1.03
W21	3	20	18.9	9	0	2	0	7	348	71	161	-	2.51	4.96	12.25	2.51	-	2.36	3.31	7.48	1.15	1.90	3.58	3.95
W22	2	7	5.4	5.7	1	1.65	-	6	294	53	143	1.53	4.48	-	5.78	1.53	1.44	4.38	-	5.37	1.00	3.81	-	3.88

Note: When there is no tensile stress in the mudstone foundation,  $Fos_{te}$  has no value. For the case of an anacinal slope, blocks do not slide and  $Fos_{st}$  has no value. Both parameters are replaced by "-".

## 310 5 Discussion

### 311 5.1 Characteristics of rock block stability

312 There are up to 12 results of  $Fos$  per potential unstable block with the consideration of three scenarios and four failure modes (i.e., partial damage and overall failure). Most  $Fos_{te}$  values are less than 1 in all scenarios (yellow points in Fig.10),  
313 except for two blocks (i.e., W17 and W20), whose  $Fos_{te}$  values are also close to 1 under rainfall or earthquake scenarios.  
314 Although most of  $Fos_{co}$  values (green points in Fig. 10) are greater than 1, they are closer to the critical state of  $Fos = 1$   
315 than  $Fos_{sl}$  and  $Fos_{to}$  (represented by blue and orange points in Fig. 10, respectively). The compression damage of the  
316 exposed mudstone can be investigated in the field survey (Fig. 4d). However, it is difficult to observe the phenomenon of  
317 tensile damage inside the mudstone base. In the case of weak tensile strength, the mudstone base suffers from tensile failure,  
318 and compression failure usually occurs before tension failure. According to the results, their  $Fos_{te}$  and  $Fos_{co}$  are less than 1  
319 or close to 1, which means that the underlying mudstone has been partially damaged due to slight compressive or tensile  
320 failure, and the blocks are potentially unstable with the current depth of the basal cavity. However, most of the blocks do not  
321 exhibit overall failure, and they still exist on the slope. Moreover, their  $Fos_{sl}$  and  $Fos_{to}$  values are greater than 1 in different  
322 scenarios, which is consistent with this actuality. The results indicate that most of the blocks are close to a critical state, in  
323 which they are partially damaged but the whole block is still stable.  
324



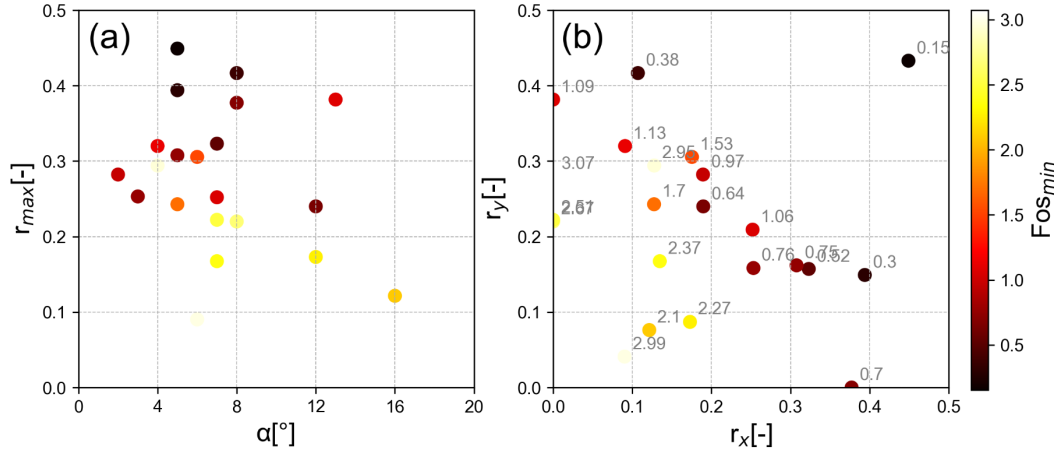
325

326 **Figure 10** Distribution of  $Fos$  in different scenarios. Shapes represent different scenarios and colours represent different failure modes.

### 327 5.2 Relationship between $Fos$ and geometric parameters

328 Fig. 11 presents the relationship between  $Fos_{min}$  and two main geometric parameters, the dip of the contact surface and the  
329 retreat ratio. In general, the dip angle of the contact surface ( $\alpha$ ) is the key factor influencing the sliding failure mode. The

330 horizontal axis in Fig. 11a is  $\alpha$  between the rock blocks and underlying mudstone. Most of the points in Fig. 11a are in the  
 331 interval  $[0, 8^\circ]$ , which is consistent with the features of sub-horizontal strata in the study area. The shade of the points does  
 332 not change significantly in the  $x$ -axis direction, as Fig. 11a shows. Therefore, compared with the maximum retreat ratio  
 333 ( $r_{max}$ ), the dip of the contact surface has less influence on rockfall stability in the study area. There was a significant positive  
 334 correlation between the retreat ratio ( $r_{max}$ ) and  $Fos_{min}$ . In Fig. 11b, as the retreat ratios increase in the positive direction of  
 335 the  $x$ -axis and  $y$ -axis, the rock blocks show a notable tendency to be unstable.



336  
 337 **Figure 11** Correlation between  $Fos$  and the dip of contact surface and retreat ratio. Here,  $\alpha$  is the dip angle of the contact surface between  
 338 rock block and underlying mudstone,  $r_x$  and  $r_y$  are the retreat ratio along  $x$  direction and  $y$  direction, respectively, equal to  $d_1/a$  and  
 339  $d_2/b$ , and  $r_{max}$  is the larger of  $r_x$  and  $r_y$ .

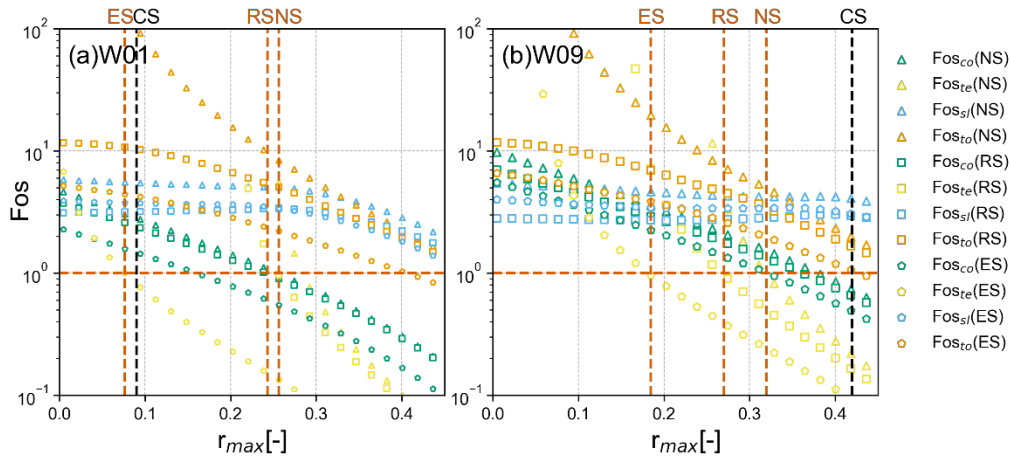
### 340 5.3 Definition of rockfall susceptibility

341 To explore the variation in  $Fos$  with the progressive erosion process of the cavity on the blocks, the cavity retreat velocities  
 342 in different directions are assumed to be equal (5 mm/year, Zhang et al. (2016)). Fig. 12 shows the variations in  $Fos$  of two  
 343 specific blocks during the evolution process of the mudstone cavity. In the initial stage, the cavity is small, and the overlying  
 344 block is stable; all  $Fos$  values are greater than 1.0. The cavity expands over time as the mudstone weathers; then, the contact  
 345 area decreases, and non-uniform distributed stress arises. When the stress exceeds the ultimate strength of mudstone in a  
 346 partial area,  $Fos_{co}$  and  $Fos_{te}$  decrease significantly, as shown in Fig. 12. The instability of the blocks starts from the failure  
 347 (or damage) of the foundation.  $Fos_{te}$  and  $Fos_{co}$  reach the critical state much earlier than  $Fos_{sl}$  and  $Fos_{to}$ . For these two  
 348 specific blocks, when  $r_{max}$  increases to 0.4,  $Fos_{sl}$  and  $Fos_{to}$  are still higher than 1.0. This means that the rock blocks can  
 349 remain globally stable in this condition.

350 These results further elucidate the stability analysis model proposed in this study.  $Fos_{co}$  and  $Fos_{te}$  introduced in this model  
 351 present the damage state of basal mudstone caused by compressive and tensile stresses, which do not provide global  
 352 instability of the overlying block as sliding and toppling. However,  $Fos_{co}$  and  $Fos_{te}$  are important preliminary signs of

353 subsequent global failure of the rock block. The damage in the basal mudstone can significantly accelerate weathering and  
 354 prompt expansion of the cavity, which will lead to global failure. The lower  $Fos_{co}$  and  $Fos_{te}$  are, the lesser the safety margin  
 355 of the blocks. Therefore, the four  $Fos$  used in this study can provide a more comprehensive quantification of rockfall  
 356 stability.

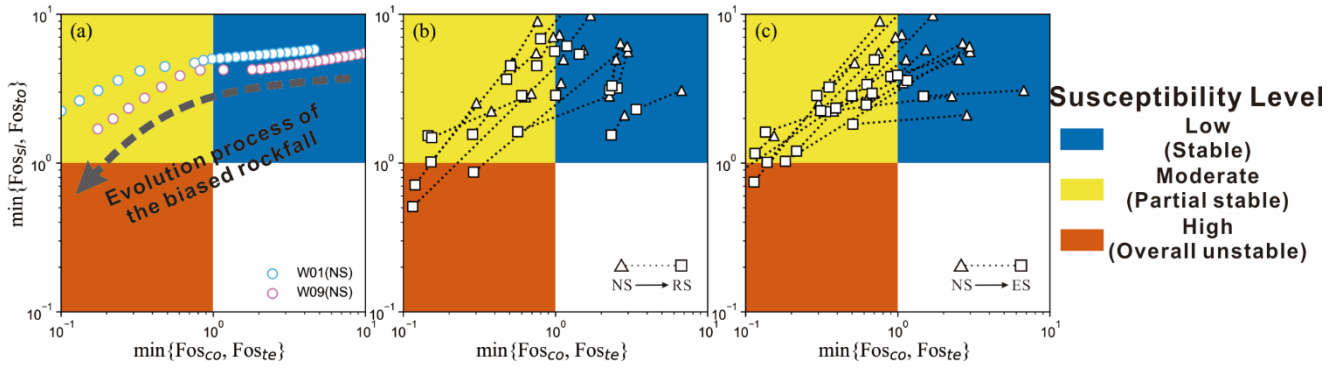
357 This result is consistent with Fig. 10, in which 63.7% of the yellow and green points ( $Fos_{te}$  and  $Fos_{co}$ ) are located between  
 358  $Fos = 0.7$  and  $Fos = 2.0$ . This result can be validated by the field phenomena. In the study area, rock damage (e.g., micro-  
 359 fractures and cleavages) can be observed in the underlying mudstone. However, most overlying rock blocks are stable at the  
 360 present time. This means that even if  $Fos_{sl}$  or  $Fos_{to}$  is higher than 1, its foundation has begun to be damaged. In the case of  
 361 heavy rain or earthquakes,  $Fos_{sl}$  and  $Fos_{to}$  may be reduced to less than 1, and the rockfall occurs.



362  
 363 **Figure 12** Variation in  $Fos$  with  $r_{max}$ . (a) and (b) are the results for W01 and W09, respectively, which represent the situation of the  
 364 blocks with two and three free faces. The black dotted line (CS) approximately represents the current state of the unstable blocks. The red  
 365 dotted lines correspond to the critical values of  $r$  in different scenarios.

366 Based on the meaning of four  $Fos$ , rockfall susceptibility can be divided into three levels. When both  $Fos_{co}$  and  $Fos_{te}$  are  
 367 greater than 1, the overall rock block is stable, and the mudstone base is not damaged, which is defined as “low susceptibility”  
 368 and represented by the blue area in Fig. 13. With the development of cavity erosion, when  $Fos_{co}$  or  $Fos_{te}$  is less than 1 and  
 369  $Fos_{sl}$  and  $Fos_{to}$  are higher than 1, the base undergoes be damaged, and the overlying sandstone blocks remain relatively  
 370 stable. This state is defined as “moderate susceptibility” and represented by the yellow area. When  $Fos_{sl}$  or  $Fos_{to}$  is less  
 371 than 1 in some scenarios, the rock blocks are in a “high susceptibility” state, which means that rockfalls are highly likely to  
 372 occur. Fig. 13a indicates that along with the increase in the cavity retreat ratio, the susceptibility of W01 and W09 changes  
 373 from low susceptibility to moderate susceptibility in the natural scenario. As Fig. 13b and c show, when rainfall or  
 374 earthquake occurs,  $Fos_{sl}$  or  $Fos_{to}$  of some blocks is less than 1, which means that some blocks have evolved to the state of  
 375 high susceptibility and the overall sandstone blocks are unstable.

376

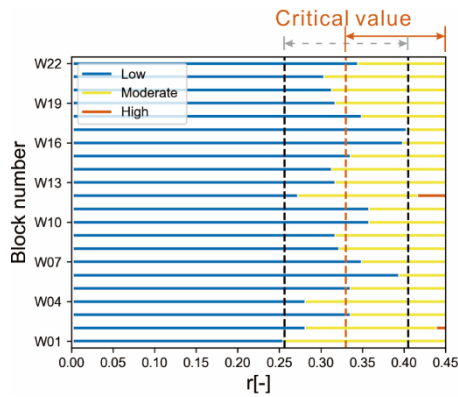


377

378 **Figure 13** Rockfall susceptibility based on the combination of four  $FOS$ . The susceptibility is defined as three levels, represented by red,  
 379 yellow and blue. (a) shows the progressive failure process of the rock block changing from low susceptibility to moderate susceptibility as  
 380 the cavity retreat ratio increases (illustrated by W01 and W09 in the natural scenario. (b) and (c) show the change in susceptibility of  
 381 biased rock blocks, when the scenario changes from natural conditions to rainfall and earthquake conditions.

#### 382 5.4 Critical retreat ratio in the study area

383 The cavity plays an important role in the progressive failure process of biased rockfall. To analyse the effect of the retreat  
 384 ratio on the stability of rock blocks, all blocks in the study area were selected to calculate their  $FOS$  and susceptibility level  
 385 with the increasing  $r$ , whose retreat velocities in different directions are assumed to be equal. Fig. 14 shows that along with  
 386 the increase in the retreat ratio, the susceptibility level of rock blocks changes from low to moderate susceptibility.  
 387 Corresponding to the critical state of  $\min\{FOS_{co}, FOS_{te}\} = 1$  of all blocks, the minimum retreat ratio is 0.26, and the  
 388 maximum retreat ratio is 0.41, as marked by the vertical black dotted line in Fig. 14. According to the statistical analysis of  
 389 critical retreat ratios, both mean and median are 0.33. Therefore, the critical retreat ratio of the rock blocks in the study area  
 390 can be determined as 0.33, which is marked by the vertical red dotted line in the Fig. 14. The critical retreat ratio calculated  
 391 by this method can be used for the preliminary identification of potential unstable rock blocks in a specific area, which can  
 392 help concentrate limited risk treatment resources on these priorities. It should be emphasized that the mechanical parameters  
 393 and analysis scenarios significantly affect the critical value. Therefore, the elaborative risk control of a given rockfall should  
 394 be arranged based on its specific parameters and analysis scenarios.



395

396 **Figure 14** Effect of the retreat ratio ( $r$ ) on the  $FoS$  of the rock block, which is illustrated by all blocks in the study area.

### 397 5.5 Limitations

398 This study involves the development of an analytical model for the three-dimensional stability of biased rockfall, combining  
 399 the basic LEM method and the consideration of the eccentricity effect. Due to the complexity of rock structure and force  
 400 analysis, it is necessary to highlight the limitations of this model.

401 First, this study uses a three-dimensional coordinate system and bending theory. It is difficult to consider diverse shapes of  
 402 rock blocks, and the rock block was simplified as a prismatic column. The assumption of fully persistent discontinuities may  
 403 underestimate the stability of rock blocks, and ignores the stress transmission in joints or rock bridges. Then, following the  
 404 basic framework of the general LEM method, this study assumed that the rock is not subjected to deformations. The  
 405 complete stress-strain behaviour, such as the deformation in the mudstone layer, is not considered in this study. Furthermore,  
 406 the block stability is strongly influenced by the uncertainty of mechanical parameters. However, because of the difficulties in  
 407 sampling strongly weathered mudstone, it is difficult to obtain adequate parameter values for uncertainty statistics. These  
 408 limitations will be important considerations in future studies.

### 409 6 Conclusion

410 Due to differential weathering in sub-horizontally interbedded of hard rock and soft rock, multi-layer biased rockfalls  
 411 develop on steep slopes. In mountainous ranges, cut slopes, and coastal cliffs, rockfall may cause significant facility damage  
 412 and casualties in residential areas and transport corridors. The aim of this study was to present a new three-dimensional  
 413 analytical method for the stability of rock blocks with basal cavities. In this method, a non-uniform distributed stress due to  
 414 the eccentricity effect is applied at the contact surface instead of a point force. The method considers four failure modes  
 415 according to the rockfall evolution process, including partial damage of the soft foundation ( $FoS_{co}$  and  $FoS_{te}$ ) and overall  
 416 failure of the rock block ( $FoS_{sl}$  and  $FoS_{to}$ ).

417 Taking the northeast edge of the Sichuan Basin in Southwest China as the study area, the proposed method is used to  
418 calculate the *Fos* of biased unstable rock blocks. The results show that in the natural scenario, the underlying mudstone of  
419 some rock blocks has been partially damaged, and compression failure of the mudstone has been observed in the field. Some  
420 rock blocks are expected to fail as a whole in rainfall or earthquake scenarios. The statistical analysis indicates that the  
421 retreat ratio is the crucial factor influencing the *Fos* of biased rockfall. On the basis of different combinations of four *Fos*,  
422 rockfall susceptibility was classified into three levels. As the retreat rate increases, the rock blocks undergo an evolution  
423 process from stability to partial instability and then overall instability. Based on the current mechanical parameters of the  
424 eastern Sichuan Basin, the critical retreat ratio from low to moderate rockfall susceptibility is 0.33.

425 The proposed method improves the three-dimensional mechanical model of a rock block with a basal cavity by considering  
426 non-uniform distributed stress at the contact surface, which could promote the accuracy of rockfall stability analysis. Due to  
427 the assumptions adopted and the complexity of the failure mechanism of biased rockfall, there are some limitations in this  
428 method, mainly including the simplification of boundary conditions and rock deformation. These limitations will be  
429 important considerations in future studies.

#### 430 **Data availability**

431 All raw data can be provided by the corresponding authors upon request.

#### 432 **Author contributions**

433 XS, BC and JD planned the campaign; XS and BC performed the field measurements; XS, BC, WW and BL designed and  
434 developed the methodology. XS, BC and JD analysed the data; XS and BC wrote the manuscript draft; JD and WW  
435 reviewed and edited the manuscript.

#### 436 **Competing interests**

437 The authors declare that they have no conflicts of interest.

#### 438 **Acknowledgements**

439 This research is funded by the National Natural Science Foundation of China (No. 42172318 and No. 42177159). The first  
440 author thanks Master Chengjie Luo and Yu Wang for data collection in the field. We also appreciate the assistance of the  
441 Research Center of Geohazard Monitoring and Warning in the Three Gorges Reservoir, China.



## 442 References

- 443 Adrian, I.: Pressures distribution for eccentrically loaded rectangular footings on elastic soils, Proceedings of the 2010  
444 international conference on Mathematical models for engineering science, Tenerife, Spain, 213–216,
- 445 Alejano, L. R., Carranza-Torres, C., Giani, G. P., and Arzua, J.: Study of the stability against toppling of rock blocks with  
446 rounded edges based on analytical and experimental approaches, *Eng. Geol.*, 195, 172-184,  
447 <https://doi.org/10.1016/j.enggeo.2015.05.030>, 2015.
- 448 Alejano, L. R., Ordóñez, C., Armesto, J., and Rivas, T.: Assessment of the instability hazard of a granite boulder, *Nat.*  
449 *Hazards*, 53, 77-95, <https://doi.org/10.1007/s11069-009-9413-0>, 2010.
- 450 Ashby, J.: Sliding and toppling modes of failure in models and jointed rock slopes, M.S. thesis, Imperial College London  
451 University, London, 1971.
- 452 Bray, J. W. and Goodman, R. E.: The theory of base friction models, *Int. J. Rock Mech. Min. Sci. Geomech. Abstr.*, 18, 453-  
453 468, [https://doi.org/10.1016/0148-9062\(81\)90510-6](https://doi.org/10.1016/0148-9062(81)90510-6), 1981.
- 454 Budetta, P.: Assessment of rockfall risk along roads, *Nat. Hazards Earth Syst. Sci.*, 4, 71-81, [https://doi.org/10.5194/nhess-4-](https://doi.org/10.5194/nhess-4-71-2004)  
455 [71-2004](https://doi.org/10.5194/nhess-4-71-2004), 2004.
- 456 Budetta, P. and Nappi, M.: Comparison between qualitative rockfall risk rating systems for a road affected by high traffic  
457 intensity, *Nat. Hazards Earth Syst. Sci.*, 13, 1643-1653, <https://doi.org/10.5194/nhess-13-1643-2013>, 2013.
- 458 Chau, K. T., Wong, R. H. C., Liu, J., and Lee, C. F.: Rockfall hazard analysis for Hong Kong based on rockfall inventory,  
459 *Rock Mech. Rock Eng.*, 36, 383-408, <https://doi.org/10.1007/s00603-002-0035-z>, 2003.
- 460 Chen, H. K. and Tang, H. M.: Stability analysis method of perilous rock in source of avalanche, *J. Geol. Min. Res.*, 2, 60-67,  
461 <https://doi.org/10.5897/JGMR.9000070>, 2010.
- 462 Chen, H. K., Xian, X. F., Tang, H. M., and Feng, Q. H.: A massive development mechanism and countermeasures for  
463 perilous rocks in the Three Gorges Reservoir area of PR China: The example of the Taibaiyan cliff at Wanzhou, *Journal of*  
464 *Chongqing University*, 31, 1178-1184, <https://doi.org/10.11835/j.issn.1000-582X.2008.10.019>, 2008.
- 465 Corominas, J., Mavrouli, O., and Ruiz-Carulla, R.: Magnitude and frequency relations: are there geological constraints to the  
466 rockfall size?, *Landslides*, 15, 829-845, <https://doi.org/10.1007/s10346-017-0910-z>, 2018.
- 467 Cruden, D. M. and Varnes, J. D.: *Landslide types and processes. Landslides: investigation and mitigation, transportation*  
468 *research board (National Research Council), National Academy Press, Washington, DC, 1996.*
- 469 D'Amato, J., Hantz, D., Guerin, A., Jaboyedoff, M., Baillet, L., and Mariscal, A.: Influence of meteorological factors on  
470 rockfall occurrence in a middle mountain limestone cliff, *Nat. Hazards Earth Syst. Sci.*, 16, 719-735,  
471 <https://doi.org/10.5194/nhess-16-719-2016>, 2016.
- 472 Derron, M. H., Jaboyedoff, M., and Blikra, L. H.: Preliminary assessment of rockslide and rockfall hazards using a DEM  
473 (Oppstadhornet, Norway), *Nat. Hazards Earth Syst. Sci.*, 5, 285-292, <https://doi.org/10.5194/nhess-5-285-2005>, 2005.

474 Ferrari, F., Giacomini, A., and Thoeni, K.: Qualitative Rockfall Hazard Assessment: A Comprehensive Review of Current  
475 Practices, *Rock Mech. Rock Eng.*, 49, 2865-2922, <https://doi.org/10.1007/s00603-016-0918-z>, 2016.

476 Frattini, P., Crosta, G., Carrara, A., and Agliardi, F.: Assessment of rockfall susceptibility by integrating statistical and  
477 physically-based approaches, *Geomorphology*, 94, 419-437, <https://doi.org/10.1016/j.geomorph.2006.10.037>, 2008.

478 Frayssines, M. and Hantz, D.: Modelling and back-analysing failures in steep limestone cliffs, *Int. J. Rock Mech. Min. Sci.*,  
479 46, 1115-1123, <https://doi.org/10.1016/j.ijrmms.2009.06.003>, 2009.

480 Guzzetti, F., Reichenbach, P., and Wieczorek, G. F.: Rockfall hazard and risk assessment in the Yosemite Valley, California,  
481 USA, *Nat. Hazards Earth Syst. Sci.*, 3, 491-503, <https://doi.org/10.5194/nhess-3-491-2003>, 2003.

482 Hutchinson, J. N.: Field and laboratory studies of a fall in Upper Chalk cliffs at Joss Bay, Isle of Thanet, in: *Stress-Strain*  
483 *Behaviour of Soils*, Proceedings of the Roscoe Memorial Symposium, Oxfordshire, 29-31 March 1971, 692-706, 1972.

484 Jaboyedoff, M., Baillifard, F., Philipposian, F., and Rouiller, J. D.: Assessing fracture occurrence using "weighted  
485 fracturing density": a step towards estimating rock instability hazard, *Nat. Hazards Earth Syst. Sci.*, 4, 83-93,  
486 <https://doi.org/10.5194/nhess-4-83-2004>, 2004.

487 Jaboyedoff, M., Ben Hammouda, M., Derron, M.-H., Guérin, A., Hantz, D., and Noel, F.: The Rockfall Failure Hazard  
488 Assessment: Summary and New Advances, in: *Understanding and Reducing Landslide Disaster Risk: Volume 1 Sendai*  
489 *Landslide Partnerships and Kyoto Landslide Commitment*, edited by: Sassa, K., Mikoš, M., Sassa, S., Bobrowsky, P. T.,  
490 Takara, K., and Dang, K., Springer International Publishing, Cham, 55-83, [https://doi.org/10.1007/978-3-030-60196-6\\_3](https://doi.org/10.1007/978-3-030-60196-6_3),  
491 2021.

492 Kogure, T., Aoki, H., Maekado, A., Hirose, T., and Matsukura, Y.: Effect of the development of notches and tension cracks  
493 on instability of limestone coastal cliffs in the Ryukyus, Japan, *Geomorphology*, 80, 236-244,  
494 <https://doi.org/10.1016/j.geomorph.2006.02.012>, 2006.

495 Kromer, R., Lato, M., Hutchinson, D. J., Gauthier, D., and Edwards, T.: Managing rockfall risk through baseline monitoring  
496 of precursors using a terrestrial laser scanner, *Can. Geotech. J.*, 54, 953-967, <https://doi.org/10.1139/cgj-2016-0178>, 2017.

497 Malamud, B. D., Turcotte, D. L., Guzzetti, F., and Reichenbach, P.: Landslide inventories and their statistical properties,  
498 *Earth Surf. Process. Landf.*, 29, 687-711, <https://doi.org/10.1002/esp.1064>, 2004.

499 Matasci, B., Stock, G. M., Jaboyedoff, M., Carrea, D., Collins, B. D., Guerin, A., Matasci, G., and Raveland, L.: Assessing  
500 rockfall susceptibility in steep and overhanging slopes using three-dimensional analysis of failure mechanisms, *Landslides*,  
501 15, 859-878, <https://doi.org/10.1007/s10346-017-0911-y>, 2018.

502 Pérez-Rey, I., Muñoz-Menéndez, M., González, J., Vagnon, F., Walton, G., and Alejano, L. R.: Laboratory physical  
503 modelling of block toppling instability by means of tilt tests, *Eng. Geol.*, 282, 105994,  
504 <https://doi.org/10.1016/j.enggeo.2021.105994>, 2021.

505 Pierson, L. A., Davis, S. A., and Van Vickie, R.: Rockfall hazard rating system—implementation manual, Federal Highway  
506 Administration (FHWA), Report FHWA—OR-EG-90-01, FHWA, US Department of Transportation, 80 pp., 1990.

507 Sagaseta, C.: On the Modes of Instability of a Rigid Block on an Inclined Plane, *Rock Mech. Rock Eng.*, 19, 261-266,  
508 <https://doi.org/10.1007/Bf01039998>, 1986.

509 Santi, P. M., Russell, C. P., Higgins, J. D., and Spriet, J. I.: Modification and statistical analysis of the Colorado Rockfall  
510 Hazard Rating System, *Eng. Geol.*, 104, 55-65, <https://doi.org/10.1016/j.enggeo.2008.08.009>, 2009.

511 Tang, H. M., Wang, L. F., Chen, H. K., and Xian, X. F.: Collapse sequence of perilous rock on cliffs with soft foundation,  
512 *Chinese Journal of Geotechnical Engineering*, 32, 205-210, 2010.

513 Volkwein, A., Schellenberg, K., Labiouse, V., Agliardi, F., Berger, F., Bourrier, F., Dorren, L. K. A., Gerber, W., and  
514 Jaboyedoff, M.: Rockfall characterisation and structural protection – a review, *Nat. Hazards Earth Syst. Sci.*, 11, 2617-2651,  
515 <https://doi.org/10.5194/nhess-11-2617-2011>, 2011.

516 Ward, D. J., Berlin, M. M., and Anderson, R. S.: Sediment dynamics below retreating cliffs, *Earth Surf. Process. Landf.*, 36,  
517 1023-1043, <https://doi.org/10.1002/esp.2129>, 2011.

518 Wu, L. Z., Zhang, L. M., Zhou, Y., Xu, Q., Yu, B., Liu, G. G., and Bai, L. Y.: Theoretical analysis and model test for  
519 rainfall-induced shallow landslides in the red-bed area of Sichuan, *Bull. Eng. Geol. Environ.*, 77, 1343-1353,  
520 <https://doi.org/10.1007/s10064-017-1126-0>, 2018.

521 Yu, B., Ma, E., Cai, J., Xu, Q., Li, W., and Zheng, G.: A prediction model for rock planar slides with large displacement  
522 triggered by heavy rainfall in the Red bed area, Southwest, China, *Landslides*, 18, 773-783, <https://doi.org/10.1007/s10346-020-01528-x>, 2021.

524 Zhan, J., Yu, Z., Lv, Y., Peng, J., Song, S., and Yao, Z.: Rockfall Hazard Assessment in the Taihang Grand Canyon Scenic  
525 Area Integrating Regional-Scale Identification of Potential Rockfall Sources, *Remote Sens.*, 14, 3021,  
526 <https://doi.org/10.3390/rs14133021>, 2022.

527 Zhang, K., Tan, P., Ma, G. W., and Cao, P.: Modeling of the progressive failure of an overhang slope subject to differential  
528 weathering in Three Gorges Reservoir, China, *Landslides*, 13, 1303-1313, <https://doi.org/10.1007/s10346-015-0672-4>, 2016.

529 Zhang, M., Yin, Y. P., and Huang, B. L.: Mechanisms of rainfall-induced landslides in gently inclined red beds in the eastern  
530 Sichuan Basin, SW China, *Landslides*, 12, 973-983, <https://doi.org/10.1007/s10346-015-0611-4>, 2015.

531 Zheng, L. N., Chen, J. B., Zhou, Q. J., Feng, S. Q., Luo, Y. B., and Shen, P.: Experimental study on bearing capacity of  
532 moderately weathered mudstone in Chengdu area, *Chinese Journal of Geotechnical Engineering*, 43, 926-932,  
533 <https://doi.org/10.11779/CJGE202105017>, 2021.

534 Zhou, C., Yin, K. L., Cao, Y., Ahmed, B., Li, Y. Y., Catani, F., and Pourghasemi, H. R.: Landslide susceptibility modeling  
535 applying machine learning methods: A case study from Longju in the Three Gorges Reservoir area, China, *Comput. Geosci.*,  
536 112, 23-37, <https://doi.org/10.1016/j.cageo.2017.11.019>, 2018.

537 Zhou, Y., Shi, S., Zhang, Y., Cai, Q., Liang, J., and Cheng, Y.: Stability of unstable rock in nearly-horizontal sandstone-  
538 mudstone stratum due to enlarged rock-cell, *Journal of Engineering Geology*, 25, 1220-1229,  
539 <https://doi.org/10.13544/j.cnki.jeg.2017.05.006>, 2017.